WILEY-VCH

In-situ synthesis of the peapod-like Cu-SnO_2@copper foam as anode with excellent cycle stability and high area specific capacity

Bobo Lu,[1,a] Wenbo Liu,[1,a,] Xiangjiang Liu,[a] Yi Gan,[a] Shichao Zhang,[b] and Sanqiang Shi[c]*

[a] School of Mechanical Engineering, Sichuan University, Chengdu 610065, China

[b] School of Materials Science and Engineering, Beihang University, Beijing 100191, China

[c] Department of Mechanical Engineering, The Hong Kong Polytechnic University, Hung Hom, Kowloon, Hong Kong

[1] These authors contributed equally to this work.

Tel: +86-028-85405320; Fax: +86-028-85403408; E-mail: liuwenbo_8338@163.com (W. Liu).

B. B. Lu, Prof. W. B. Liu, Y. Gan, X. J. Liu
School of Mechanical Engineering
Sichuan University
Chengdu 610065, China
E-mail: liuwenbo_8338@163.com (W. Liu)

Prof. S. C. Zhang
School of Materials Science and Engineering
Beihang University
Beijing 100191, China

Prof. S. Q. Shi
Department of Mechanical Engineering
The Hong Kong Polytechnic University
Hung Hom, Kowloon, Hong Kong 999077

Abstract: The theoretical specific capacity of tin oxide (SnO_2) anode material is more than twice that of graphite material (782 *vs.* 372 mAh g^{-1}), whereas its potential usage is limited fatally by huge volume expansion during lithiation. An effective solution is to encapsulate tin oxide into hollow structure such as yolk-shell based on the principle of confinement. However, in light of the restricted space of active substance, this kind of hollow electrode always has the low capacity, severely limiting its commercial value. Herein, we tactfully design and construct a peapod-like Cu-SnO_2@copper foam (CF) as high area specific capacity anode based on the Kirkendall effect, in which the "pod and peas" in the peapod-like structure are composed of SnO_2 and Cu nanoparticles, respectively. Compared to other SnO_x-based electrodes with different hollow structure designs in published reports, the unique peapod-like Cu-SnO_2@CF anode delivers a remarkably high first reversible capacity of 5.80 mAh cm^{-2} as well as excellent cycle stability with 66.7% capacity retention and ca. 100% coulombic efficiency after 200 cycles at a current density of 1 mA cm^{-2}, indicative of its quite promising application toward high-performance lithium-ion batteries.

1. Introduction

In recent years, the rapid development of new energy automobile industry has expanded dramatically the application market of lithium-ion batteries (LIBs). The long cycle life and high capacity requirements make the commercial graphite anode material (372 mAh g^{-1}) not meet the urgent demand in the future industry.[1-3] As a result, the study of high-performance anode materials has always been a research hotspot.[4-6] The tin oxide (SnO_2) reacting with Li can form Li_2Sn_5, LiSn, $Li_{22}Sn_5$ and other alloys, in which the theoretical specific capacity of SnO_2 to $Li_{22}Sn_5$ is as high as 782 mAh g^{-1}, more than twice that of graphite material.[7,8] However, when SnO_2 is directly used as anode material for LIBs, its volume changes would

surpass 200% during the charge-discharge processes.[9,10] The huge internal mechanical stress from volume expansion can quickly destroy electrode structure, resulting in the decrease of electrical conductivity and capacity attenuation.[11-13] To solve this issue, the common strategy is to build the nanostructure of SnO_2. The small feature size and large specific surface area can effectively alleviate volume changes, shorten ion transport distances and provide more electrochemical active sites, which is beneficial to the enhancement of Li storage performance.[14-16] Nevertheless, nano-sized SnO_2 would be largely apt to reaggregate, pulverize and fall off due to the thermodynamics instability and lack of sufficient space to accommodate the volume expansion during cycling. In order to further improve the cycle stability of SnO_2, the strategy to design the hollow structure is proposed accordingly.[17,18]

Compared to dense structure, the hollow SnO_2 has larger specific surface area and higher surface activity, which can greatly promote the electrochemical reaction; at the same time, the cavity in hollow structure can effectively accommodate the volume expansion and avoid the collapse of electrode structure caused by the huge internal mechanical stress.[19] The hollow core-shell,[20-22] yolk-shell[23,24] and peapod-like[25,26] structures designed based on the principle of confinement are three kinds of typical patterns, which usually encapsulate SnO_2 into hollow carbon shell. The cycle stability of SnO_2 can be improved largely by use of good conductivity of carbon shell and the constraint effect of hollow structure on active material. However, due to the restricted space of SnO_2 and the low capacity of carbon, the Li storage capability of this type of hollow electrode is always undesirable, severely limiting its commercial value.[27-29]

For example, N. Wu et al.[22] reported the novel SnO_{2-x}/N-rGO (N-doped reduced graphene oxide) nanocomposites with hollow nanosphere structures synthesized by electrostatic

adsorption-induced self-assembly along with thermal reduction, in which the N-rGO networks are coated on the hollow SnO_2 nanospheres. The SnO_{2-x}/N-rGO as anode material for LIBs delivered a charge specific capacity of 0.78 mAh cm^{-2} and ca. 55.3% capacity retention after 120 cycles at a current density of 0.65 mA cm^{-2}, indicative of its low capacity and poor cycle stability. Y. Wang et al.[26] designed and prepared the hollow core-shell SnO_2/CNTs (carbon nanotubes) composites through confined-space catalytic deposition assisted by a hard template, i.e. anodic aluminium oxide (AAO) membrane. The hollow core-shell SnO_2/CNTs as anode material for LIBs displayed a reversible capacity of only 0.33 mAh cm^{-2} after 200 cycles at a current density of 0.3 mA cm^{-2}. Obviously, the preparation process is complicated and the electrochemical performance is unsatisfactory, which needs to be further improved. As is well-known, SnO_2 and other metal oxides (Fe_2O_3, SiO_2, etc.) can be prepared into composites to boost its electrical conductivity via the formation of heterojunction.[30-32] Compared to metal oxides, a large number of reports show that the combination of SnO_2 and carbon can bring about the better properties.[33,34] It is worth noting that the conductivity of Cu is normally several orders of magnitude higher than that of carbon.[35,36] Therefore, it can be reasonable to predict that the incorporation of Cu into SnO_2 would facilitate the further enhancement of electrochemical performance.

Different from traditional hollow SnO_2 electrodes, herein, we tactfully design and construct a peapod-like Cu-SnO_2@copper foam (CF) based on the principle of the Kirkendall effect, in which the “pod and peas” in the peapod-like structure are composed of SnO_2 and Cu nanoparticles (NPs), respectively. There are many merits in such a unique peapod-like products. Firstly, the ample cavity inside the “peapod” can greatly alleviate the huge volume expansion during lithiation. Secondly, the peapod-like Cu-SnO_2 can further improve the Li

storage capability because of unrestricted space of SnO_2. Thirdly, the Cu NPs like rivets dispersing in the hollow SnO_2 form a connected internal conductive network, promoting the electron migration inside the electrode. Fourthly, the Cu-SnO_2 in-situ grown on 3D CF with good mass transfer channels can achieve a better mechanical bond between active material and substrate than the coated electrode, which is conducive to the fast ion transport and improvement of structure stability.

As a result, the as-made peapod-like Cu-SnO_2@CF electrode in this work can further boost the electrochemical properties compared to other SnO_x-based electrodes with different hollow structure designs in published reports. The unique peapod-like anode can deliver a remarkably high first reversible capacity of 5.80 mAh cm^{-2} as well as excellent cycle stability with 66.7% capacity retention and ca. 100% coulombic efficiency after 200 cycles at a current density of 1 mA cm^{-2}. This work is of great significance to the in-situ synthesis of high-performance lithium-ion battery anodes with novel hollow structures based on the Kirkendall effect.

2. Results and Discussion

Figure 1 shows a schematic diagram of in-situ synthesis of the peapod-like Cu-SnO_2@CF electrode. Briefly, Cu_2O nanorods can be prepared firstly on 3D CF surface by two-step heat treatments based on the Ostwald ripening theory,[37] and then they were replaced further into the hollow Cu_2O-SnO_2 by the Kirkendall effect.[38-40] Finally, the hollow Cu_2O-SnO_2 was reduced thoroughly to the peapod-like Cu-SnO_2 on 3D CF in a sulfuric acid solution. For the resultant peapod-like Cu-SnO_2@CF, the Cu NPs like peas dispersing in the hollow SnO_2 shell form a connected internal conductive network, thus promoting the electron migration inside the electrode compared with the hollow Cu_2O-SnO_2@CF before chemical reduction. Besides, SnO_2 as a single active substance in the electrode is more beneficial to deeply study its

electrochemical lithiation/delithiation mechanism as well as further avoid the extra volume expansion caused by the cuprous oxide.

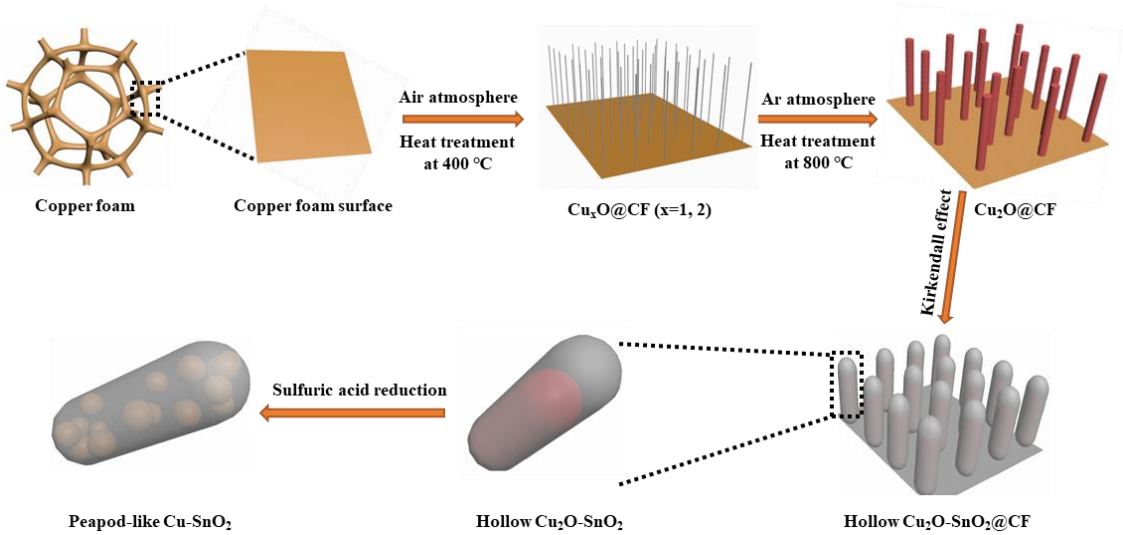

Figure 1. Schematic diagram of in-situ synthesis of the peapod-like Cu-SnO_2@CF electrode.

The formation mechanism of the hollow Cu_2O-SnO_2 based on the Kirkendall effect is illustrated further in Figure S1. Specifically, during the electrochemical replacement, Cu^+ on the surfaces of Cu_2O nanorods is replaced by Sn^{4+} in the solution to form the SnO_2 shell, and the replaced Cu^+ and Cl^- combine to form the CuCl, which can be dissolved in the Cl^--rich solution. Driven by the concentration gradient of Cu^+ in the solution and the electromotive force between Cu^+ and Sn^{4+}, the Cu^+ and O^{2-} of Cu_2O inside the SnO_2 shell can continually spread to the solution, leading to the generation of the Kirkendall vacancies in their original positions.[41,42] Meanwhile, the Sn^{4+} in the solution gradually diffuses into the SnO_2 shell from outside to inside under the action of electromotive force.[42,43] As the Kirkendall vacancies largely converge, the hollow Cu_2O-SnO_2 with cavity can be formed eventually. The detailed reaction processes can be expressed as follows:

$$SnCl_4 + xH_2O + 2Cu_2O \rightarrow SnO_2 \cdot xH_2O + 4CuCl \quad (1)$$

$$CuCl + (x\text{-}1)Cl^- \rightarrow [CuCl_x]^{1-x} \quad (2)$$

Scanning electron microscopy (SEM) was carried out to characterize the microstructure and morphology of the products at different stages. Obviously, Cu_xO (x=1, 2) nanowires with a length of 4~5 μm are evenly distributed on the surface of CF by the 1st-step heat treatment, as shown in **Figure 2a-c**. The morphology, size and density of Cu_xO nanowires on the CF matrix can be tuned easily by changing the temperature and heating rate of heat treatment. The density and length of the nanowires increase initially and afterwards decrease with the raise of the heating rate (Figure S2a-e). Note that the concentration of the nanowires at 450 ℃ is much higher than that at 400 ℃ for the same holding time (8 h) at the constant heating rate of 10 ℃/min (Figure S2f). Furthermore, the uniformly dispersed Cu_2O nanorods can be successfully obtained on the 3D substrate by the 2nd-step heat treatment, as presented in **Figure 2d-f**. Similarly, the morphology, size and density of the nanorods on the matrix also can be adjusted effectively by changing the temperature and holding time of heat treatment. At 800 ℃, the diameter of the nanorods by the heat treatment for 4 h is slightly larger than that for 2 h (Figure S3a-b). This is mainly due to atoms quickly diffusing at high temperatures, and thus the longer the holding time is, the larger the nanorods grow. At 900 ℃ for 2 h, we can observe some voids appearing in the matrix, which is because after Cu atoms in the matrix diffusing into the nanorods, the vacancies left behind quickly aggregate and finally form them (Figure S3c). Note that the length of the nanorods is ca. 1~4 μm. **Figure 2g-i** shows the microstructure of the hollow Cu_2O-SnO_2@CF obtained by the Kirkendall effect. Clearly, the prepared hollow structure with a length of 1~4 μm well inherits the feature size of the previous nanorods by comparing **Figure 2e** and **Figure 2h**. In order to effectively improve the electron transfer ability of electrode and obtain the single active substance of SnO_2, the hollow Cu_2O-SnO_2 was further reduced to the peapod-like Cu-SnO_2 on 3D CF in a sulfuric

acid solution **(Figure 2j-l)**. The XRD patterns of the peapod-like Cu-SnO_2@CF electrodes by sulfuric acid reduction with different concentrations are displayed in Figure S4. Evidently, as the concentration of sulfuric acid solution is slightly increased, it is easy to reduce the Cu_2O to Cu completely in the products.

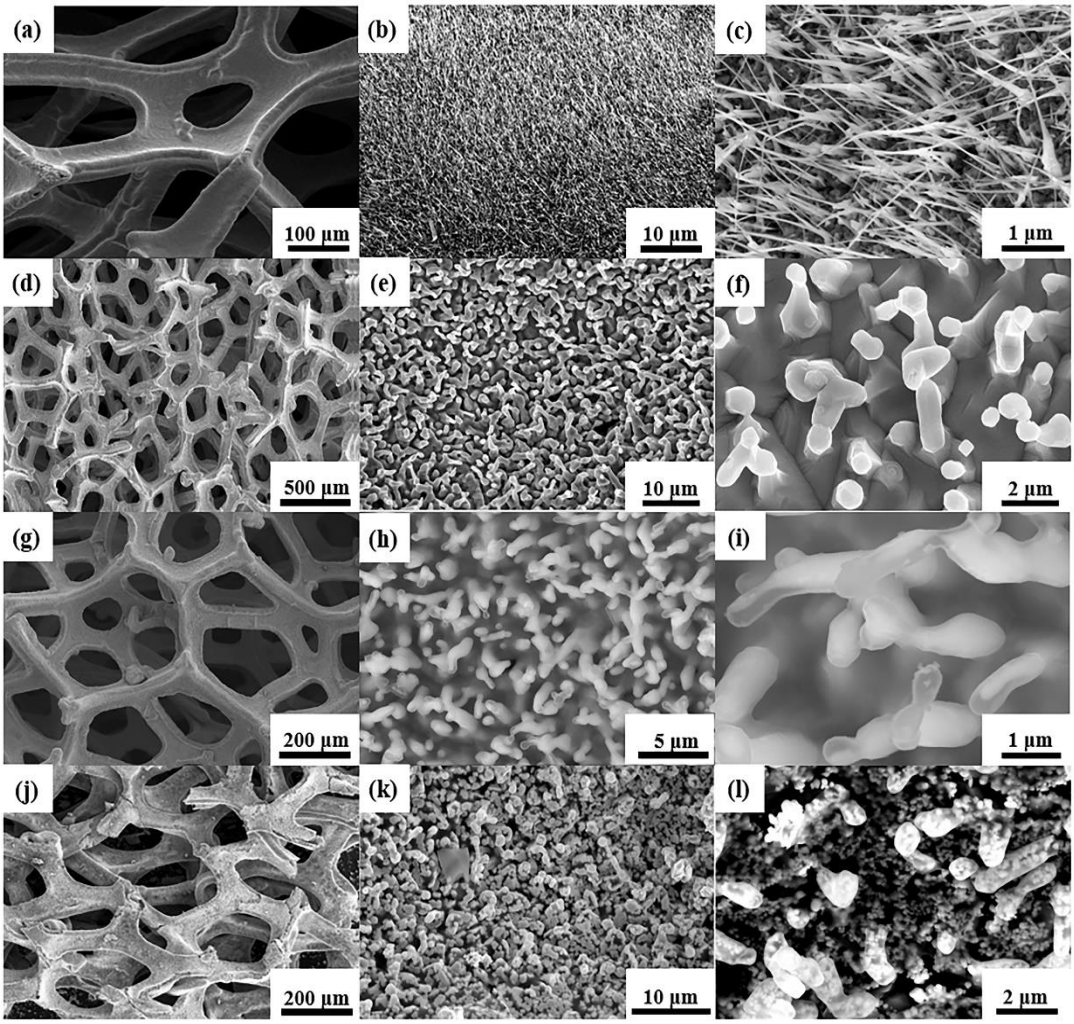

Figure 2. SEM images of a-c) the Cu_xO@CF (x=1, 2) electrode by the 1st-step heat treatment at 400 ℃ for 8 h in air atmosphere, d-f) the Cu_2O@CF electrode by the 2nd-step heat treatment at 800 ℃ for 4 h in Ar atmosphere, g-j) the hollow Cu_2O-SnO_2@CF electrode obtained by the Kirkendall effect, k-m) the peapod-like Cu-SnO_2@CF electrode reduced in a 0.7 mol/L sulfuric acid solution.

In the transmission electron microscopy (TEM) images of **Figure 3a** and Figure S5a-b, the peapod-like Cu-SnO_2 can be clearly observed. The thickness of the hollow SnO_2 shell is ca. 20~30 nm, and the Cu NPs like peas are inside the hollow structure, as marked by the red dotted circles. Also, the dispersed NPs can be observed in Figure S5c-d and their sizes can be

determined to be ca. 50~80 nm. **Figure 3b** shows the high-resolution TEM (HRTEM) image of the hollow shell pointed out by the white rectangle in Figure 3a. Obviously, there exist two kinds of lattice spacing: 0.22 and 0.34 nm, corresponding to (200) and (110) crystal planes of SnO_2 respectively.[15] Note that the crystallinity of SnO_2 is relatively low and there is only a small amount of crystallization, indicating its dominated amorphous nature. In **Figure 3c-g**, it can be found that Sn and O elements are evenly distributed in the hollow shell, while the Cu element only exists in the dispersed NPs and the matrix, as characterized clearly by elemental mapping of the peapod-like Cu-SnO_2@CF.

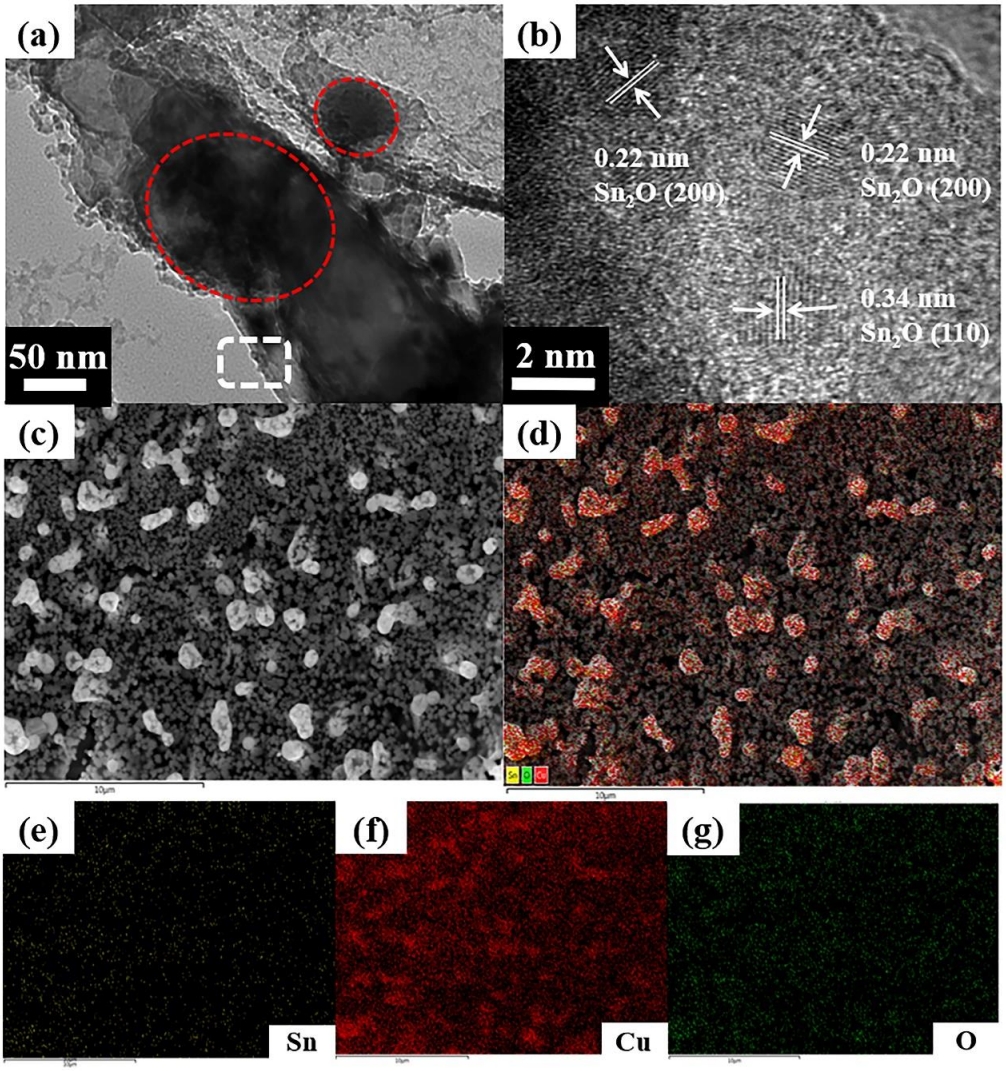

Figure 3. a-b) TEM and HRTEM images of the peapod-like Cu-SnO_2, in which the red dotted circles show the Cu NPs and the white rectangle corresponds to the HRTEM image magnified in part b. c-g) Elemental mapping images of the peapod-like Cu-SnO_2@CF electrode.

X-ray diffraction (XRD) and energy dispersive X-ray (EDX) analysis were performed to identify the phase structure and chemical composition of the products at different stages. **Figure 4a** shows the nanowires@CF in Figure 2a-c consisting of copper oxide, cuprous oxide and copper, suggesting that the nanowires grown on the CF matrix are composed of CuO (ICDD card no. 44-0706) and Cu_2O (ICDD card no. 05-0667) hybrids upon the 1st-step heat treatment. **Figure 4b** presents the nanorods@CF in Figure 2d-f comprising cuprous oxide and copper, indicating that upon the 2nd-step heat treatment all the copper oxide are converted to cuprous oxide and the nanorods are composed of single Cu_2O (ICDD card no. 05-0667). **Figure 4c** displays the hollow structure@CF in Figure 2g-i simultaneously containing tin oxide, cuprous oxide and copper, manifesting that the hollow structure on the CF matrix is composed of SnO_2 and residual Cu_2O inside after the incomplete electrochemical replacement based on the Kirkendall effect. Note that the headmost broad peak in Figure 4c corresponds to the amorphous SnO_2,[44-46] which is in good line with the HRTEM results in Figure 3b. **Figure 4d** exhibits the peapod-like structure@CF in Figure 2j-l involving amorphous tin oxide and copper, implying that upon the further chemical reduction, the residual Cu_2O has almost completely converted into the dispersed Cu NPs in the hollow structure. Additionally, EDX characterization was carried out for the hollow Cu_2O-SnO_2@CF and peapod-like Cu-SnO_2@CF electrodes, as shown in Figure S6. It is clear that both spectra 1 and 2 contain Sn and O elements, further confirming the shells in the hollow structure and peapod-like structure are composed of SnO_2 after the electrochemical replacement and chemical reduction in combination of the XRD and HRTEM results, respectively.

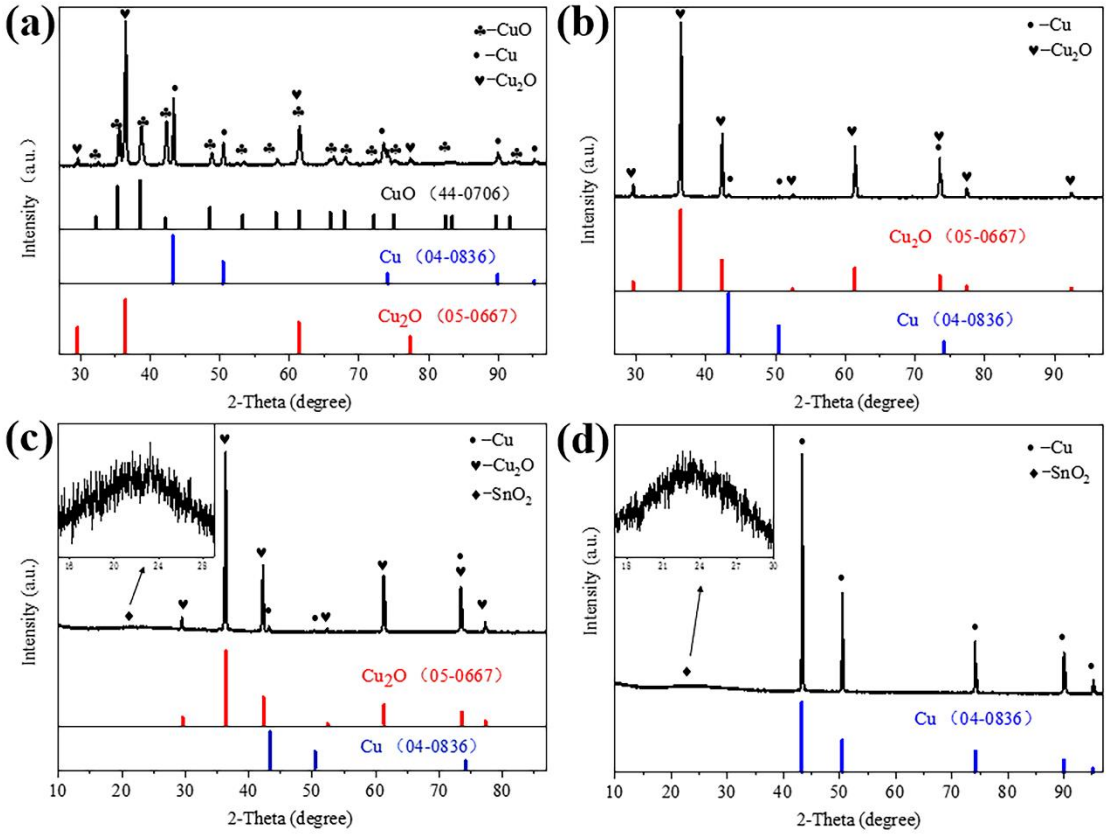

Figure 4. XRD patterns of a) the Cu_xO@CF (x=1, 2), b) the Cu_2O@CF, c) the hollow Cu_2O-SnO_2@CF, d) the peapod-like Cu-SnO_2@CF electrodes.

The X-ray photoelectron spectroscopy (XPS) was further conducted to detect the chemical states of the peapod-like Cu-SnO_2@CF electrode reduced in a 0.7 mol/L sulfuric acid solution. The XPS survey spectrum in **Figure 5a** shows the coexistence of Sn, Cu and O elements in the products, which match well with the previous EDX results. For the high-resolution XPS spectrum of Sn 3d orbitals in **Figure 5b**, the two peaks at 494.916 and 486.5 eV correspond to the Sn $3d_{3/2}$ and Sn $3d_{5/2}$ peaks in the binding energy between Sn^{4+} and O,[47,48] in which the binding energy difference of 8.416 eV between them is highly consistent with the counterpart between Sn $3d_{3/2}$ and Sn $3d_{5/2}$ of Sn^{4+} in SnO_2.[49-51] Both of the two peaks of Sn 3d orbitals have good symmetry, further suggesting the shell in the peapod-like structure is composed of single SnO_2. Similarly, in the high-resolution XPS spectrum of Cu 2p **(Figure 5c)**, there are

four fitting peaks located at 953.0, 951.6, 933.2 and 931.8 eV, respectively. Among them, both the 953.0 and 933.2 eV designate to the Cu^0, which is in good agreement with the above XRD results. The 951.6 and 931.8 eV correspond to the Cu $2p_{1/2}$ and Cu $2p_{3/2}$ peaks of Cu^+ in Cu_2O.[52-55] The present results indicate that a trace amount of unreduced Cu_2O still remains in the products even if it cannot be detected by XRD under its detection limit. However, the unreduced Cu_2O just can be regarded as an impurity in the peapod-like Cu-SnO_2@CF electrode, which hardly contributes to the available capacity due to its extremely low content. In addition, note that the conventional X-ray radiation sources (Al K_α) are not completely monochromatic but have small companion lines of slightly higher energy (K_β, etc.), thus resulting in the small companion peaks in the XPS spectrum in addition to the main peaks excited by K_α.[56-58]

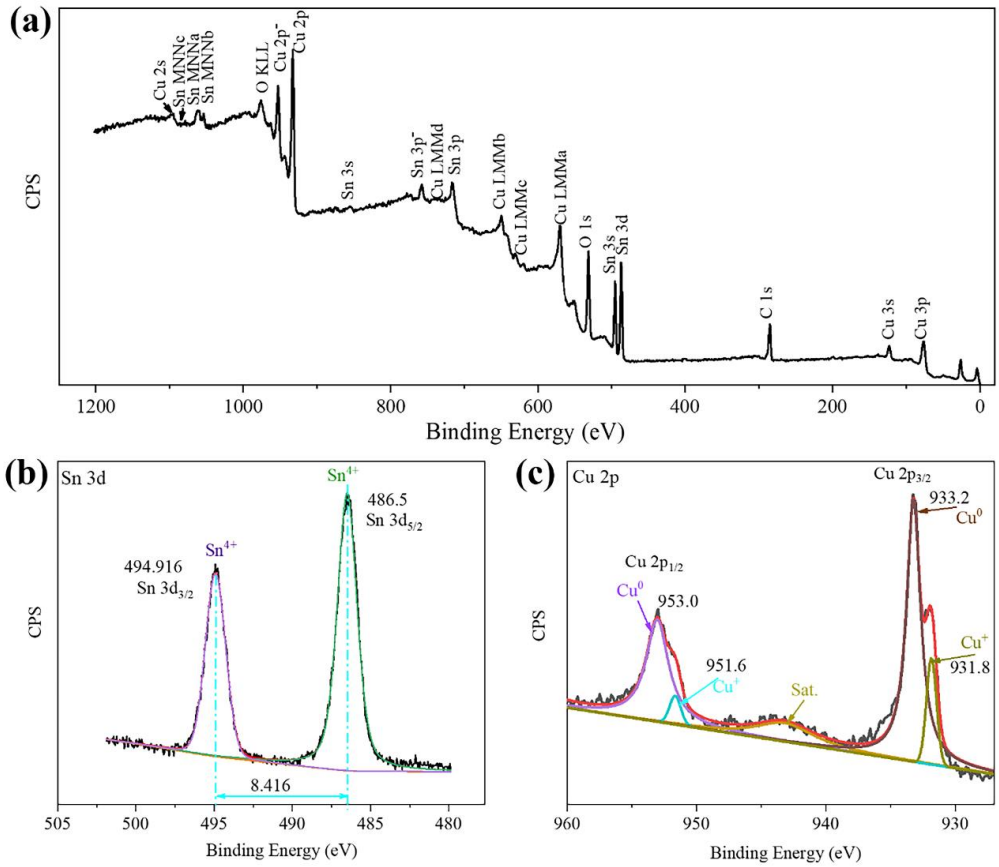

Figure 5. a) XPS survey spectrum of the peapod-like Cu-SnO_2@CF electrode. b-c) High-resolution XPS spectra of Sn 3d and Cu 2p for the peapod-like Cu-SnO_2@CF electrode.

Subsequently, the peapod-like Cu-SnO_2@CF electrode directly as a binder-free integrated anode for LIBs were systematically investigated to evaluate its Li storage performance. The CVs for the first three cycles are tested to reveal its electrochemical lithiation-delithiation mechanism, as shown in **Figure 6a**, in which the open circuit voltage (OCV) is ca. 1.48 V (vs. Li/Li^+). Clearly, there is a quite broad reduction peak from ca. 1.25 to 0.30 V (vs. Li/Li^+) in the 1st discharge process, which is closely related to the formation of solid electrolyte interface (SEI) films from the decomposition of organic electrolyte on electrode surfaces, the generation of Sn NPs and amorphous Li_2O from SnO_2 reduction as well as the alloying reaction of Sn with Li to form Li_xSn ($0 < x < 4.4$).[59,60] The broad oxidation peak centered at 0.890 V (vs. Li/Li^+) in the 1st charge process is relevant to the dealloying reaction of the Li_xSn alloy into Sn and Li.[22,61] During the succeeding discharge processes, the steady reduction peak of 0.547 V (vs. Li/Li^+) merely corresponds to the single reversible transformation of Sn to Li_xSn ($0 < x < 4.4$).[62,63] Obviously, the relatively large capacity loss in the 1st-cycle CVs is mainly associated with the irreversible formation of SEI films and amorphous Li_2O. In **Figure 6b**, the potential vs. capacity profiles exhibit two broad plateaus at ca. 1.0 and 0.4 V (vs. Li/Li^+) in the 1st discharge process, confirming the occurrence of multiple electrochemical reactions existing in the broad reduction peak of the 1st-cycle CVs; just an obvious plateau at ca. 0.6 V (vs. Li/Li^+) can be observed in the 2nd and 3rd discharge processes, which is in good line with the results of the 2nd- and 3rd-cycle CVs. Note that the charge process curves for the first three cycles are very similar, with a plateau located at ca. 0.9 V (vs. Li/Li^+) well corresponding to the dealloying reaction of the Li_xSn alloy ($0 < x < 4.4$). To sum up, the electrochemical lithiation-delithiation mechanism of SnO_2 in the peapod-like Cu-SnO_2@CF

electrode during the charge-discharge processes mainly includes two reaction steps as follows:

$$SnO_2 + 4Li^+ + 4e^- \rightarrow Sn + 2Li_2O \quad (3)$$

$$Sn + xLi^+ + xe^- \leftrightarrow Li_xSn \ (0 < x < 4.4) \quad (4)$$

Figure 6c displays the galvanostatic charge-discharge curves of the peapod-like Cu-SnO_2@CF electrode at a current density of 1 mA cm^{-2}; meanwhile, the hollow Cu_2O-SnO_2@CF electrode was also tested as a comparison under the same conditions. The 1st charge capacity of the hollow Cu_2O-SnO_2@CF electrode is 5.80 mAh cm^{-2}, greater than that of the peapod-like Cu-SnO_2@CF electrode (4.018 mAh cm^{-2}). This is because the Cu_2O in the hollow Cu_2O-SnO_2@CF electrode can also act as effective active material to contribute the extra capacity except for SnO_2 itself. Interestingly, the reversible capacity of the peapod-like Cu-SnO_2@CF electrode exceeds that of the hollow electrode just after 20 cycles, which is closely related to the existence of Cu_2O simultaneously increasing the volume expansion of electrode during lithiation, thus resulting into the decrease of structure stability and fast capacity decay in the hollow electrode. Moreover, the metallic Cu has markedly higher conductivity than Cu_2O, and the Cu NPs like peas dispersing in the hollow SnO_2 form a connected internal conductive network, promoting the electron migration inside the electrode. As a result, the sufficient reduction of Cu_2O to Cu can significantly improve the conductivity of electrode as well as further avoid the extra volume expansion from Cu_2O. It is worth mentioning that the designed peapod-like Cu-SnO_2@CF electrode still delivers a markedly high reversible capacity of 2.72 mAh cm^{-2} as well as excellent cycle stability with 66.7% capacity retention and ca. 100% coulombic efficiency after 200 cycles. More importantly, except for the first several cycles, the coulombic efficiency of the peapod-like electrode is

always above 99.8%, indicative of its good electrochemical reversibility, which is rarely seen in common SnO_x-based electrodes to the best of our knowledge.[64-66] Additionally, a detailed comparison of Li storage performance of various SnO_x-based electrodes with different structure designs reported in the recent literature has been listed in Table S1. Evidently, the higher area specific capacity and better cycling ability can be achieved in the peapod-like Cu-SnO_2@CF electrode.

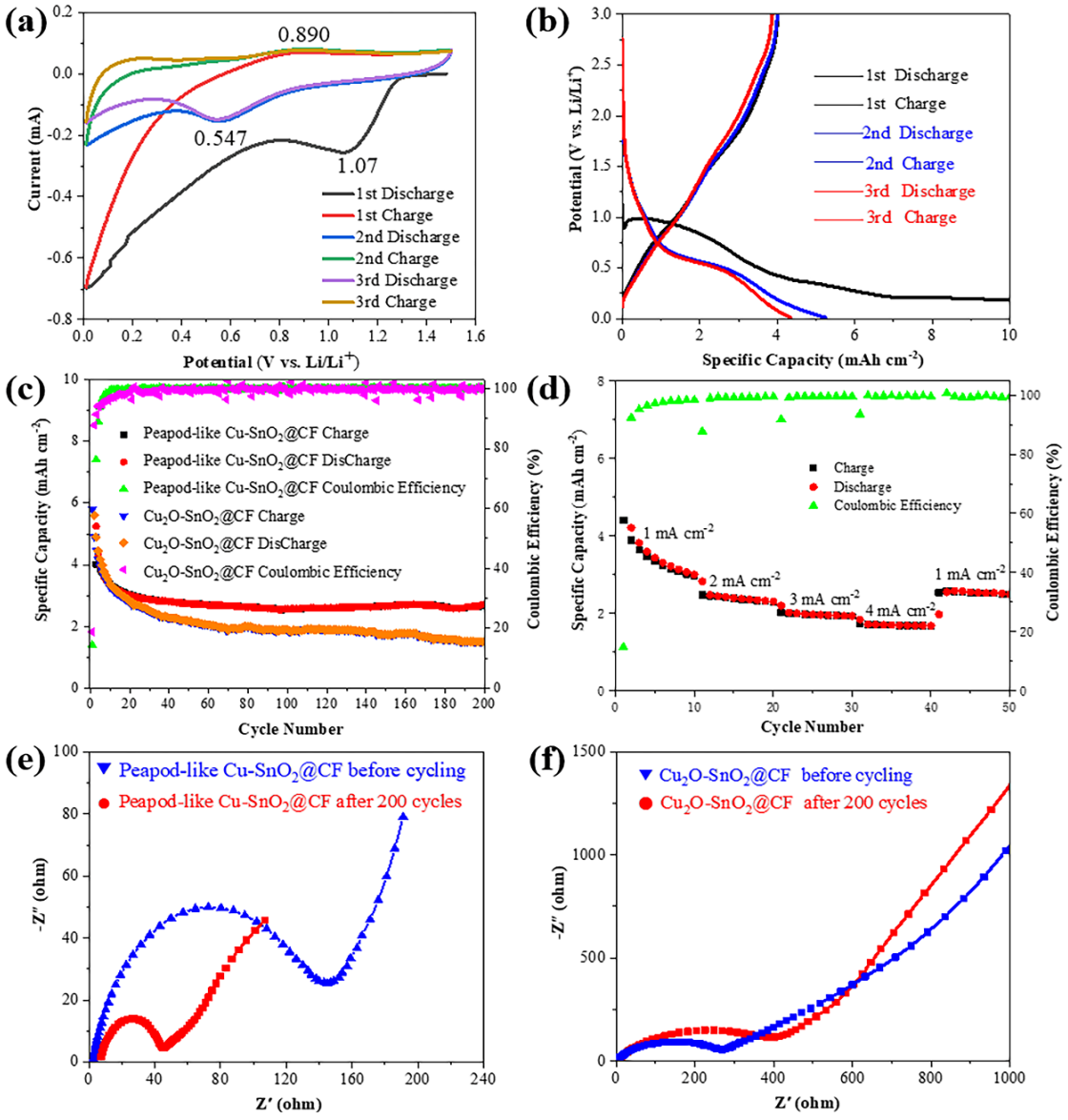

Figure 6. a) First three-cycle CVs of the peapod-like Cu-SnO_2@CF electrode ranging from 0.01 to 1.5 V (vs. Li/Li^+) at a scan rate of 0.1 mV s^{-1}. b) Potential vs. capacity profiles of the peapod-like Cu-SnO_2@CF electrode at a current density of 1 mA cm^{-2}. c) Cycle performance curves of the hollow Cu_2O-SnO_2@CF and peapod-like Cu-SnO_2@CF electrodes at a current density of 1 mA cm^{-2}. d) Rate capability profiles of the peapod-like

Cu-SnO_2@CF electrode at current densities of 1, 2, 3 and 4 mA cm^{-2}. e-f) Nyquist plots of the peapod-like Cu-SnO_2@CF and hollow Cu_2O-SnO_2@CF electrodes before and after 200 cycles.

As presented in **Figure 6d,** the rate capability of the peapod-like Cu-SnO_2@CF electrode was further studied at different current densities, which is another key index for the evaluation of Li storage properties. Clearly, the relatively large reversible capacities of 4.40, 2.47, 2.01, 1.72 and 2.53 mAh cm^{-2} can be obtained for the 1^{st}, 11^{th}, 21^{st}, 31^{st} and 41^{st} cycles at the current densities of 1, 2, 3, 4 and 1 mA cm^{-2}, respectively. With the increase of current density, the capacity of electrode decreases to some extent, which is related to the limitation of charge transport process. It should be noted, however, that when the current density returns to 1 mA cm^{-2} again, the reversible capacity can quickly increase, maintaining as high as 86.05% capacity retention compared to that of the 10^{th} cycle at the same current density, demonstrating the superior rate performance of the peapod-like Cu-SnO_2@CF electrode. This can be mainly ascribed to the synergistic effect between hollow SnO_2 shell and interior Cu conductive network promoting the charge transport kinetics at electrode/electrolyte and current collector/active material interfaces. This will be further discussed on a basis of the results of electrochemical impedance spectroscopy (EIS) in the following section.

The ion and electron transports of the peapod-like Cu-SnO_2@CF and hollow Cu_2O-SnO_2@CF electrodes were investigated by EIS, as displayed in **Figure 6e-f**. It is obvious that all Nyquist plots consist of a semicircle in the high-medium frequency range, the diameter of which represents the charge transfer resistance and an inclined line in the low frequency range closely related to the diffusion coefficient of Li^+ inside electrode materials.[67-70] Comparing Figure 6e and Figure 6f, it can be found easily that the charge transfer resistance of the peapod-like Cu-SnO_2@CF electrode always is significantly smaller

than the counterpart of the hollow electrode regardless of before or after cycling. Especially, the charge transfer resistance of the peapod-like electrode after 200 cycles is just ca. 48 Ω, far less than that before cycling (ca. 160 Ω). This is mainly because the dispersive distribution of Cu NPs like peas in the hollow SnO_2 form a connected internal conductive network, promoting the electron migration inside the electrode. In contrast, the charge transfer resistance of the hollow electrode after 200 cycles (ca. 500 Ω) is pronouncedly increased relative to that before cycling (ca. 300 Ω), suggesting the occurrence of large structure destruction in the hollow Cu_2O-SnO_2@CF electrode caused by the volume expansion during the repeated charge-discharge processes. Besides, the charge transfer resistance of the peapod-like Cu-SnO_2@CF electrode before cycling is also notably lower than those of the single SnO_2@CF and Cu_2O@CF electrodes in addition to the hollow Cu_2O-SnO_2@CF one (Figure S7), further demonstrating that the introduction of dispersed Cu NPs in the hollow SnO_2 can effectively improve the electron migration ability of the electrode, substantially responsible for the excellent electrochemical properties.

3. Conclusion

In summary, we tactfully designed and constructed a peapod-like Cu-SnO_2@CF electrode based on the Kirkendall effect, in which the peapod-like Cu-SnO_2 is composed of hollow SnO_2 shell as a "pod" and interior Cu NPs as "peas". When directly used as a binder-free integrated anode for LIBs, the unique peapod-like Cu-SnO_2@CF electrode displays the superior Li storage properties with a remarkably high first reversible capacity of 5.80 mAh cm^{-2} as well as excellent cycle stability with 66.7% capacity retention and ca. 100% coulombic efficiency after 200 cycles at 1 mA cm^{-2}. The outstanding electrochemical performance can be attributed to the following respects. Firstly, the ample cavity inside the

"peapod" can effectively accommodate the huge volume expansion and alleviate the mechanical strains during repeated lithiation-delithiation processes. Secondly, the peapod-like Cu-SnO_2 can improve the Li storage capability because of more electrochemical active sites and less space limitation of hollow SnO_2 with large specific surface area. Thirdly, the Cu NPs like peas dispersing in the hollow SnO_2 form a connected internal conductive network, promoting the electron migration inside the electrode. Fourthly, the Cu-SnO_2 in-situ grown on 3D CF with good mass transfer channels can achieve a robust mechanical bond between active material and substrate as well as further avoid the use of binders and conductive agents compared to the coated electrode, resulting in the enhanced structure stability and fast ion transport. We believe that this work will has significant inspirations for the in-situ synthesis of high-performance lithium-ion battery anodes with novel hollow structures based on the principle of the Kirkendall effect.

4. Experimental Section

4.1. Experimental Details

Synthesis of the Cu_2O@CF electrode: The commercial CF (0.8 mm×0.8 mm, ca. 1.6 mm in thickness) was cleaned by dilute sulfuric acid solution firstly to remove the surface oxide layers and then the 1st-step heat treatment with different process parameters was carried out in air atmosphere in a tube furnace, leading to the in-situ growth of Cu_xO (x=1, 2) nanowires on 3D CF (named the Cu_xO@CF electrode). Subsequently, the Cu_xO@CF electrode was further subjected to the 2nd-step heat treatment in Ar atmosphere under different process parameters in a tube furnace in order to convert the Cu_xO nanowires into the Cu_2O nanorods on 3D CF (named the Cu_2O@CF electrode).

Synthesis of the hollow Cu_2O-SnO_2@CF electrode: The as-prepared Cu_2O@CF electrode

was placed in a mixture of 10 mL absolute ethyl alcohol and 0.3 mL NaCl aqueous solution with the concentration of 100 g/L, and then the 10 mL $SnCl_4 \cdot 5H_2O$ alcohol solution with the concentration of 0.7 g/L was dropped into the above mixed solution with continuous stirring for 2~5 min. The Cu_2O nanorods on 3D CF can be replaced into the hollow Cu_2O-SnO_2 on 3D CF based on the Kirkendall effect (named the hollow Cu_2O-SnO_2@CF electrode). Upon the electrochemical replacement, the samples were rinsed with deionized water and dehydrated alcohol for several times, then dried at 70 ℃ for 24 h in vacuum oven.

Synthesis of the peapod-like Cu-SnO_2@CF electrode: The as-synthesized hollow Cu_2O-SnO_2@CF electrode was further immersed in a sulfuric acid solution with different concentrations for 20 min to fully reduce the Cu_2O in the hollow Cu_2O-SnO_2 to Cu NPs, in which the Cu NPs like peas dispersing in the hollow SnO_2 shell form a connected internal conductive network, eventually resulting in the in-situ formation of the peapod-like Cu-SnO_2 on 3D CF (named the peapod-like Cu-SnO_2@CF electrode). After the reduction reaction, the samples were also rinsed with deionized water and dehydrated alcohol for several times, then dried at 70 ℃ for 24 h in vacuum oven, and finally kept in a vacuum chamber to avoid further oxidation.

4.2. Structure Characterization

The microstructure and chemical composition of the as-synthesized Cu_xO@CF, Cu_2O@CF, hollow Cu_2O-SnO_2@CF and peapod-like Cu-SnO_2@CF electrodes were characterized by using X-ray diffraction (XRD, Rigaku D/Max-2400) with Cu K_α radiation (λ=1.5406 Å), field emission scanning electron microscopy (FESEM, Hitachi S-4800) with an EDX analyzer, transmission electron microscopy (TEM, JEOL JEM 2100F) and high-resolution transmission electron microscopy (HRTEM, JEOL JEM 2100F). The X-ray photoelectron spectroscopy

(XPS) were recorded on AXIS Ultra DLD with Al K_α radiation source (hν=1486.6 eV).

4.3. Electrochemical Measurements

The as-made hollow Cu_2O-SnO_2@CF and peapod-like Cu-SnO_2@CF electrodes was assembled in coin-type test cells (CR2032) in an Ar-filled glove box (LS-750D, DELLIX) with the lithium metal foil (Φ15.6 mm) as both the counter and reference electrodes, respectively. In the half-cells, 1 M $LiPF_6$ in ethylene carbonate (EC), dimethyl carbonate (DMC) and diethyl carbonate (DEC) (1:1:1 by v/v/v) was used as the electrolyte, and a polypropylene (PP) microporous film (Cellgard 2300) was used as the separator. The dosage of electrolyte in each half-cell is ca. 0.06 ml. The galvanostatic charge-discharge tests were conducted using a multichannel battery program-control test system (NEWARE BTS-610, Neware Technology Co., Ltd, China) at a current density of 1 mA cm^{-2} for a cut-off potential of 0.01-3.0 V (vs. Li/Li^+) at room temperature (25±1℃). Cyclic voltammograms (CVs) was recorded using a CHI 760E electrochemical workstation between 0.01 to 1.5 V (vs. Li/Li^+) at a scan rate of 0.1 mV s^{-1}. Electrochemical impedance spectroscopy (EIS) was measured in a frequency range from 0.01 Hz to 1 MHz with an AC amplitude of 5 mV.

Supporting Information

Supporting Information is available from the Wiley Online Library or from the author.

Acknowledgments

B. Lu and W. Liu contributed equally to this work. This work was financially supported by the National Natural Science Foundation of China (52075351, 51604177), the National Key Research and Development Program of China (2019YFA0705701), the International S&T Innovation Cooperation Program of Sichuan Province (2020YFH0039), the Chengdu International S&T Cooperation Funded Project (2019-GH02-00015-HZ,

2020-GH02-00006-HZ), the "1000 Talents Plan" of Sichuan Province, the Experimental Technology Project of Sichuan University (SCU201078), and the Talent Introduction Program of Sichuan University (YJ201410). Additionally, the authors specially thank Dr. Shanling Wang (Analytical & Testing Center, Sichuan University) for help in TEM characterization.

Conflict of Interest

The authors declare no conflict of interest.

Data Availability Statement

The data that support the findings of this study are available from the corresponding author upon reasonable request.

Keywords

peapod-like structure, Cu-SnO_2@copper foam, in-situ synthesis, high area specific capacity, the Kirkendall effect

Received: ((will be filled in by the editorial staff))
Revised: ((will be filled in by the editorial staff))
Published online: ((will be filled in by the editorial staff))

References

[1] J. Liu, Y. Wen, P. A. van Aken, J. Maier, Y. Yu, *Nano Lett.* **2014**, *14*, 6387.

[2] J. Deng, C. Yan, L. Yang, S. Baunack, S. Oswald, H. Wendrock, Y. Mei, O. G. Schmidt, *ACS Nano* **2013**, *7*, 6948.

[3] Q. Xu, H. Xue, S. Guo, *Electrochim. Acta* **2018**, *292*, 1.

[4] S. Guo, J. Li, J. Xiao, H. Xue, *ACS Appl. Mater. Interfaces* **2017**, *9*, 37694.

[5] Q. Xu, J. Li, H. Xue, S. Guo, *J. Power Sources* **2018**, *396*, 675.

[6] W. B. Liu, L. Chen, L. Cui, J. Z. Yan, S. C. Zhang, S. Q. Shi, *J. Mater. Chem. A* **2019**, *7*, 15089.

[7] L. Wang, D. Wang, Z. Dong, F. Zhang, J. Jin, *Nano Lett.* **2013**, *13*, 1711.

[8] R. Liu, W. Su, P. He, C. Shen, C. Zhang, F. Su, C. Wang, *J. Alloy Compd.* **2016**, *688*, 908.

[9] S. Ding, X. W. Lou, *Nanoscale* **2011**, *3*, 3586.

[10] H. Kim, J. Cho, *J. Mater. Chem.* **2008**, *18*, 771.

[11] M. Liu, S. Zhang, H. Dong, X. Chen, S. Gao, Y. Sun, W. Li, J. Xu, L. Chen, A. Yuan, W. Lu, *ACS Sustain. Chem. Eng.* **2019**, *7*, 4195.

[12] C. Guan, X. Wang, Q. Zhang, Z. Fan, H. Zhang, H. J. Fan, *Nano Lett.* **2014**, *14*, 4852.

[13] X. Liu, Y. Han, J. Zeng, H. Yang, K. Zhou, D. Pan, *J. Mater. Sci.-Mater. Electron.* **2018**, *29*, 5710.

[14] G. D. Park, J. Lee, Y. C. Kang, *Adv. Funct. Mater.* **2017**, *27*, 1603399.

[15] W. Zhang, P. Cao, L. Li, K. Yang, K. Wang, S. Liu, Z. Yu, *Chem. Eng. J.* **2018**, *348*, 599.

[16] B. Cao, Z. Liu, C. Xu, J. Huang, H. Fang, Y. Chen, *J. Power Sources* **2019**, *414*, 233.

[17] G. Wu, H. Wu, K. Wang, C. Zheng, Y. Wang, A. Feng, *RSC Adv.* **2016**, *6*, 58069.

[18] B. Ma, B. Lu, J. Luo, X. Deng, Z. Wu, X. Wang, *Electrochim. Acta* **2018**, *288*, 61.

[19] Y. Lin, J. Duh, M. Hung, *J. Phys. Chem. C* **2010**, *114*, 13136.

[20] H. Guo, R. Mao, D. Tian, W. Wang, D. Zhao, X. Yang, S. Wang, *J. Mater. Chem. A* **2013**, *1*, 3652.

[21] H. Zhang, H. Song, X. Chen, J. Zhou, H. Zhang, *Electrochim. Acta* **2012**, *59*, 160.

[22] R. Liu, D. Li, C. Wang, N. Li, Q. Li, X. Lü, J.S. Spendelow, G. Wu, Nano Energy 2014, 6, 73.

[23] Y. Wang, J. Yang, S. Chou, H. K. Liu, W. Zhang, D. Zhao, S. X. Dou, *Nat. Commun.* **2015**, *6*, 8689.

[24] J. S. Cho, Y. C. Kang, *Small* **2015**, *11*, 4673.

[25] H. Yu, Y. Zhang, L. Dong, J. Wang, *Mat. Sci. Semicon. Proc.* **2021**, *121*, 105451.

[26] L. Yang, S. Li, J. Liu, K. Zhu, S. Liu, M. Lei, *J. Mater. Chem. A* **2017**, *5*, 1629.

[27] L. Protesescu, A. J. Rossini, D. Kriegner, M. Valla, A. de Kergommeaux, M. Walter, K. V. Kravchyk, M. Nachtegaal, J. Stangl, B. Malaman, P. Reiss, A. Lesage, L. Emsley, C. Copéret, M. V. Kovalenko, *ACS Nano* **2014**, *8*, 2639.

[28] X. Wang, M. Feygenson, M. C. Aronson, W. Han, *J. Phys. Chem.C* **2010**, *114*, 14697.

[29] K. Wang, Y. Huang, M. Yu, X. Qin, *J. Alloy Compd.* **2017**, *698*, 547.

[30] F. Li, G. Luo, J. Yu, W. Huang, D. Xu, W. Chen, X. Huang, S. Yang, Y. Fang, X. Yu, *J. Alloy Compd.* **2019**, *773*, 778.

[31] L. Zhang, H. B. Wu, S. Madhavi, H. H. Hng, X. W. Lou, *J. Am. Chem. Soc.* **2012**, *134*, 17388.

[32] D. Gulevich, M. Rumyantseva, A. Marikutsa, T. Shatalova, E. Konstantinova, E. Gerasimov, A. Gaskov, *Materials* **2019**, *12*, 3618.

[33] X. Ao, J. Jiang, Y. Ruan, Z. Li, Y. Zhang, J. Sun, C. Wang, *J. Power Sources* **2017**, *359*, 340.

[34] J. Qin, N. Zhao, C. Shi, E. Liu, F. He, L. Ma, Q. Li, J. Li, C. He, *J. Mater. Chem. A* **2017**, *5*, 10946.

[35] W. Chen, S. Maloney, W. Wang, *Nanotechnology* **2016**, *27*, 415401.

[36] Y. Jiang, Y. Wan, W. Jiang, H. Tao, W. Li, S. Huang, Z. Chen, B. Zhao, *Chem. Eng. J.* **2019**, *367*, 45.

[37] J. S. Cho, J. S. Park, Y. C. Kang, *Sci. Rep.* **2016**, *6*, 38933.

[38] S. W. Chee, S. F. Tan, Z. Baraissov, M. Bosman, U. Mirsaidov, *Nat. Commun.* **2017**, *8*, 1224.

[39] Y. Sun, Y. Xia, *Science* **2002**, *298*, 2176.

[40] X. Lu, L. Au, J. McLellan, Z. Li, M. Marquez, Y. Xia, *Nano Lett.* **2007**, *7*, 1764.

[41] C. M. Cobley, Y. Xia, *Mater. Sci. Eng. R* **2010**, *70*, 44.

[42] Z. Wang, D. Luan, F. Y. Boey, X. W. Lou, *J. Am. Chem. Soc.* **2011**, *133*, 4738.

[43] J. Azevedo, M. P. Fernández-García, C. Magén, A. Mendes, J. P. Araújo, C. T. Sousa, *Sci. Rep.* **2019**, *9*, 11994.

[44] L. Fan, X. Li, B. Yan, X. Li, D. Xiong, D. Li, H. Xu, X. Zhang, X. Sun, *Appl. Energ.* **2016**, *175*, 529.

[45] Y. Yu, L. Gu, A. Dhanabalan, C. Chen, C. Wang, *Electrochim. Acta* **2009**, *54*, 7227.

[46] S. Fan, J. Zhang, X. Teng, X. Wang, H. Li, Q. Li, J. Xu, D. Cao, S. Li, H. Hu, *J. Electrochem. Soc.* **2019**, *166*, A3072.

[47] D. Cheng, J. Liu, X. Li, R. Hu, M. Zeng, L. Yang, M. Zhu, *J. Power Sources* **2017**, *350*, 1.

[48] D. Zuo, S. Song, C. An, L. Tang, Z. He, J. Zheng, *Nano Energy* **2019**, *62*, 401.

[49] H. Wang, Q. Pan, Q. Wu, X. Zhang, Y. Huang, A. Lushington, Q. Li, X. Sun, *J. Mater. Chem. A* **2017**, *5*, 4576.

[50] M. Liu, Y. Liu, Y. Zhang, Y. Li, P. Zhang, Y. Yan, T. Liu, *Sci. Rep.* **2016**, *6*, 31496.

[51] N. Tsud, V. Johánek, I. Stará, K. Veltruská, V. Matolín, *Thin Solid Films* **2001**, *391*, 204.

[52] W. B. Liu, P. Xiang, X. Dong, H. B. Yin, H. Yu, P. Cheng, S. C. Zhang, S. Q. Shi, *Compos. Part B-Eng.* **2021**, https://doi.org/10.1016/j.compositesb.2021.108883.

[53] X. Qiu, M. Miyauchi, K. Sunada, M. Minoshima, M. Liu, Y. Lu, D. Li, Y. Shimodaira, Y. Hosogi, Y. Kuroda, K. Hashimoto, *ACS Nano* **2012**, *6*, 1609.

[54] W. B. Liu, P. Cheng, X. M. Yan, H. M. Gou, S. C. Zhang, S. Q. Shi, *ACS Sustain. Chem. Eng.* **2021**, *9*, 4363.

[55] C. Li, Y. Su, S. Zhang, X. Lv, H. Xia, Y. Wang, *Biosens. Bioelectron.* **2010**, *26*, 903.

[56] Y. Yang, C. Tian, J. Wang, L. Sun, K. Shi, W. Zhou, H. Fu, *Nanoscale* **2014**, *6*, 7369.

[57] X. Qiu, M. Miyauchi, K. Sunada, M. Minoshima, M. Liu, Y. Lu, D. Li, Y. Shimodaira, Y. Hosogi, Y. Kuroda, K. Hashimoto, *ACS Nano* **2012**, *6*, 1609.

[58] S. Wang, Q. Huang, X. Wen, X. Li, S. Yang, *Phys. Chem. Chem. Phys.* **2002**, *4*, 3425.

[59] J. Kong, S. Y. Wong, Y. Zhang, H. R. Tan, X. Li, X. Lu, *J. Mater. Chem.* **2011**, *21*, 15928.

[60] L. Ding, S. He, S. Miao, M. R. Jorgensen, S. Leubner, C. Yan, S. G. Hickey, A. Eychmüller, J. Xu, O. G. Schmidt, *Sci. Rep.* **2015**, *4*, 4647.

[61] L. Liu, M. An, P. Yang, J. Zhang, *Sci. Rep.* **2015**, *5*, 9055.

[62] L. Zou, L. Gan, R. Lv, M. Wang, Z. Huang, F. Kang, W. Shen, *Carbon* **2011**, *49*, 89.

[63] H. Liu, R. Hu, W. Sun, M. Zeng, J. Liu, L. Yang, M. Zhu, *J. Power Sources* **2013**, *242*, 114.

[64] W. B. Liu, X. Chen, J. Z. Zhang, S. C. Zhang, S. Q. Shi, *Chem. Eng. J.* **2021**, *412*, 128591.

[65] K. Kim, W. Kim, S. Hong, *Nanoscale* **2019**, *11*, 13494.

[66] C. Chang, Y. Chen, C. Huang, Y. H. Su, C. Hu, *Electrochim. Acta* **2013**, *99*, 69.

[67] S. Deki, K. Akamatsu, T. Yano, M. Mizuhata, A. Kajinami, *J. Mater. Chem.* **1998**, *8*, 1865.

[68] W. B. Liu, X. Chen, P. Xiang, S. C. Zhang, J. Z. Yan, N. Li, S. Q. Shi, *Nanoscale* **2019**, *11*, 4885.

[69] W. Z. Wang, G. H. Wang, X. S. Wang, Y. J. Zhan, Y. K. Liu, C. L. Zheng, *Adv. Mater.* **2002**, *14*, 67.

[70] X. Dong, W. B. Liu, X. Chen, J. Z. Yan, N. Li, S. Q. Shi, S. C. Zhang, X. S. Yang, *Chem. Eng. J.* **2018**, *350*, 791.